Editors' Suggestion

Reconfigurable lateral anionic heterostructures in oxide thin films via lithographically defined topochemistry

Benjamin M. Lefler,[1] Tomáš Duchoň,[2] Goran Karapetrov,[3,1] Jiayi Wang,[1] Claus M. Schneider,[2,4] and Steven J. May[1,*]

[1]*Department of Materials Science and Engineering, Drexel University, Philadelphia, Pennsylvania 19104, USA*

[2]*Peter-Grünberg-Institut 6, Forschungszentrum Jülich GmbH, Jülich, 52425, Germany*

[3]*Department of Physics, Drexel University, Philadelphia, Pennsylvania 19104, USA*

[4]*Department of Physics, University of California Davis, Davis, California 95616, USA*

(Received 11 March 2019; published 8 July 2019)

Laterally structured materials can exhibit properties uniquely suited for applications in electronics, magnetoelectric memory, photonics, and nanoionics. Here, a patterning approach is presented that combines the precise geometric control enabled by lithography with topochemical anionic manipulation of complex oxide films. Utilizing oxidation and fluorination reactions, striped patterns of $SrFeO_{2.5}/SrFeO_3$, $SrFeO_{2.5}/SrFeO_2F$, and $SrFeO_3/SrFeO_2F$ have been prepared with lateral periodicities of 200, 20, and 4 μm. Coexistence of the distinct chemical phases is confirmed through x-ray diffraction, optical and photoemission microscopies, and optical spectroscopy. The lateral heterostructures exhibit highly anisotropic electronic transport and also enable transience and regeneration of patterns through reversible redox reactions. This approach can be broadly applied to a variety of metal-oxide systems, enabling chemically reconfigurable lateral heterostructures tailored for specific electronic, optical, ionic, thermal, or magnetic functionalities.

DOI: 10.1103/PhysRevMaterials.3.073802

I. INTRODUCTION

Given their diverse array of functional properties hosted in structurally similar but chemically distinct materials, complex oxide heterostructures have remained a major focus of materials research over the last two decades [1]. While the formation of heterointerfaces and superlattice structures can be readily achieved along a single growth direction with thin-film deposition techniques [2–4], many thin-film devices rely on laterally patterned materials. Examples of applications that currently utilize or would benefit from incorporation of in-plane heterostructures include photonic metamaterials [5,6] and plasmonic structures [7], phononic heat-guiding structures [8], two-dimensional electronics [9,10], Josephson devices [11], magnetic anisotropy control [12], magnetic recording media [13,14], rectifying junctions [15], and ionic shuttles such as in fuel cells and batteries [16]. However, a central challenge to the realization of lateral heterostructures is the difficulty in maintaining distinct crystalline phases while also achieving precise geometric control. Previous demonstrations of in-plane heterostructures have tended to address one but not both of these obstacles. For example, precise spatial control of the two-dimensional electron gas at the $LaAlO_3/SrTiO_3$ interface has been achieved laterally at the nanometer scale using scanning-probe-based direct writing [17,18]. Similar scanning probe techniques have been used to generate conductive domains on the surface of bare strontium titanate at the micron length scale [19]. Alternatively, lateral patterning of the conductive domains in the $LaAlO_3/SrTiO_3$ system has also been realized through combining electron-beam lithography and ion-beam exposure [20,21]. Masked ion implantation has been implemented in manganite thin films to generate micromagnets and artificial spin-ice lattices [22], with exposure to the ion beam inducing a ferromagnetic to paramagnetic transition within the film [23]. Ion implantation has also been used to spatially control morphotropic phases in $BiFeO_3$ thin films [24], alter magnetic anisotropy in $CoFe_2O_4$ films [25], and improve ferroelectric switching in $PbTiO_3$ by suppressing leakage currents [26]. In systems incorporating chemically immiscible phases, vertically aligned nanocomposites of separate oxide phases with stochastic geometry from phase separation have been realized that exhibit multiferroic behavior [27,28], novel magnetic properties [29,30], enhanced ionic mobility in the vertical nanoscale channels [16], and improved oxygen exchange kinetics [31]. These two-phase systems attain heterogeneity through spontaneous phase separation, offering modest size and shape control achieved through tuning the strain state, growth temperature, and the energetics of the growth process [29,32,33]. While these examples highlight the potential of lateral heterostructures to enable novel functionality by spatially confining electronic or magnetic behavior or by forming a high density of vertical interfaces, synthetic approaches that are broadly applicable and allow precise geometric control are still needed.

In this work, we present an approach to create lateral anionic heterostructures derived from perovskite oxide thin films *via* topotactic chemical reactions. The technique relies on the incorporation of O^{2-} and F^- ions into lithographically defined areas of oxygen-deficient films via postgrowth topochemical vapor transport reactions. We demonstrate the synthetic strategy by creating thin films with lateral stripes of $SrFeO_{2.5}/SrFeO_3$, $SrFeO_{2.5}/SrFeO_2F$, and $SrFeO_3/SrFeO_2F$. The heterostructures are realized through topochemical

*Corresponding author: smay@drexel.edu

modification of strontium ferrate, $SrFeO_{3-\delta}$ (SFO), thin films. This material system is chosen due to the diverse physical properties that it exhibits depending on the nominal iron oxidation state, which can be altered by tuning oxygen deficiency, δ. As a function of oxygen stoichiometry, bulk SFO ranges from a cubic, helical magnet with metallic conductivity at $\delta = 0$, to a brownmillerite, insulating G-type antiferromagnet ($T_N \sim 700$ K) with a $\sim$2.2−eV band gap at $\delta = 0.5$ [34–41]. In ferrate thin films, the oxygen content can be rapidly and reversibly manipulated through temperature and oxygen pressure [38,42]. Furthermore, the tunability of properties due to oxygen stoichiometry is expedited by the high ionic mobility within vacancy-ordered channels in the brownmillerite structure ($\delta = 0.5$) [43–45], which facilitates low-temperature topochemistry. Alternatively, fluoride ions can be incorporated into SFO films using fluoropolymer-based gas-phase topotactic reactions [46,47]. Upon fluorine inclusion by this method, there is a lattice expansion [48] as well as fluorine content-dependent resistivity and band-gap tuning [49,50], with robust antiferromagnetism reported in bulk $SrFeO_2F$ [51]. Using the SFO-based patterns as model systems, we show how the lateral heterostructures can host chemically distinct phases with disparate electronic and optical properties while enabling control of the feature sizes and geometries over lithographically accessible length scales. Additionally, the use of spatially confined topochemical transformations maintains lateral heteroepitaxy and offers reconfigurable capability through redox processes. The implications of this approach extend beyond SFO, as we anticipate that the synthetic strategy demonstrated here is transferable to a range of complex oxide films and topochemical reactions, potentially enabling new families of lateral superstructures.

II. EXPERIMENTAL

A. Thin-film synthesis

$SrFeO_{2.5}$ thin films were grown *via* oxygen-assisted molecular beam epitaxy on (001)-oriented $(LaAlO_3)_{0.3}(Sr_2TaAlO_6)_{0.7}$ (LSAT) substrates. During film deposition, the Sr source (99.95%, dendritic pieces, Alfa Aesar) was heated to $\sim$480 °C and the Fe source (99.95%, slug, Alfa Aesar) was heated to $\sim$1200 °C. Precise source temperatures varied slightly and were dictated by deposition rates calibrated by a quartz crystal microbalance before each film growth. The substrate growth temperature was held at $\sim$600 °C, and the oxygen pressure was maintained at $\sim 3 \times 10^{-6}$ Torr within the deposition chamber. Films were grown to 60 unit cells ($\sim$24 nm). Postgrowth anionic manipulation was performed in a horizontal furnace using quartz tubes (Fig. S1, Supplemental Material [52]). To realize $SrFeO_3$, films were exposed to a mixture of $\sim$5% O_3 in O_2 produced by an ozone generator, flowed at $\frac{3}{4}$ LPM, and heated to $\sim$150 °C for 1 h. Throughout this work we refer to $SrFeO_{2.5}$ and $SrFeO_3$, with these designations denoting the insulating phase ($\delta \approx 0.5$) and the metallic phase ($\delta \approx 0$). However, there is uncertainty in the exact oxygen content within the different phases of the heterostructures as we do not have a means to directly measure δ. For fluorination, samples were placed in an aluminum-foil-lined quartz boat with pellets of poly(vinylidene fluoride) (PVDF, Sigma-Aldrich) upstream of the sample, with the boat enveloped by foil and inlet and outlet holes punctured at the ends to allow for Ar carrier gas to flow through the reaction space. Samples were heated to $\sim$250 °C for 1 h.

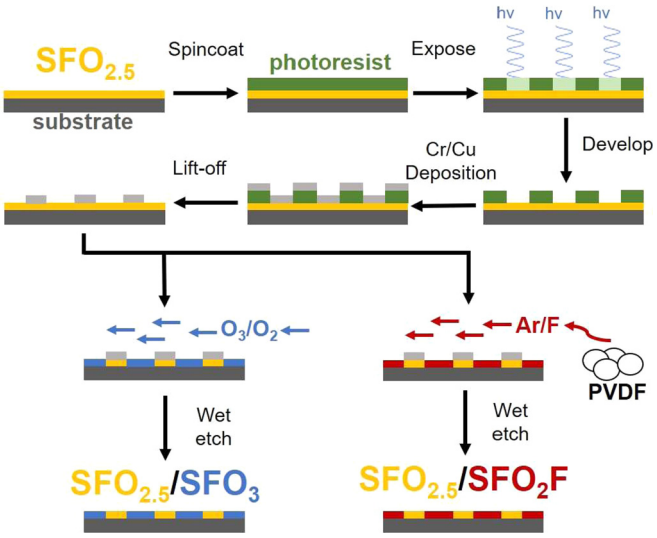

FIG. 1. Fabrication process for achieving oxide lateral heterostructures. A hard mask is lithographically defined on a film of $SFO_{2.5}$ (spin coating, exposure, developing, deposition, and lift-off). This is followed by either an ozone anneal to achieve the $SFO_{2.5}/SFO_3$ heterostructure or a fluorination reaction to achieve the $SFO_{2.5}/SFO_2F$ heterostructure. A wet etch removes the mask.

B. Heterostructure fabrication

Films were patterned using optical lithography in a process outlined in Fig. 1. $SrFeO_{2.5}$ films were spin-coated with $\sim$0.5-μm-thick Shipley S1805 positive photoresist (4000 RPM, 60 s), and soft-baked at $\sim$115 °C for 60 s. The resist was exposed in patterns by direct writing, on a Heidelberg DWL66+ laser lithography system operating at a wavelength of 355 nm, 200 mW power at 60% intensity, with 50% and 12.5% filters, and using a 10-mm writehead. After exposure, patterns were developed in Microposit MF-319 for 60 s while agitated. Samples were then hard baked at $\sim$115 °C for 60 s and cleaned in oxygen plasma using an Anatech SCE-106 barrel asher, operating at 30 sccm O_2 and 150 W for 60 s. Chromium was deposited ($\sim$100 nm), either by thermal evaporation or e-beam evaporation (interchangeably), in a Lesker PVD 75 system. Alternatively, copper was deposited ($\sim$100 nm) by thermal evaporation in a Lesker Nano-36 system. Lift-off was performed in acetone using an ultrasonication bath for 15 min. To obtain $SrFeO_3/SrFeO_{2.5}$ lateral heterostructures, Cr-masked films were exposed to ozone in the manner described above, followed by a wet etch of the Cr using Chromium Etch 1020AC (Transene). To obtain $SrFeO_{2.5}/SrFeO_2F$ heterostructures, Cr- or Cu-masked films were exposed to fluorine via decomposition of PVDF in the manner described above, followed by a wet etch of the Cr or Cu (Copper Etchant -100, Transene) and subsequent ozone anneal to obtain the oxidized $SrFeO_3/SrFeO_2F$ heterostructure.

C. Film characterization

Film thickness and crystalline quality were characterized by x-ray diffraction (XRD) and reflectivity (XRR) using a Rigaku SmartLab diffractometer with a double bounce monochromator. Diffraction and reflectivity data were modeled using GENX [53]. Photoemission electron microscopy (PEEM) and x-ray absorption spectroscopy (XAS) were performed using the FE-LEEM P90 AC instrument commercialized by SPECS and installed as a permanent end-station at the soft x-ray undulator beamline UE56/1-SGM at the synchrotron facility BESSY-II in Berlin. The samples were investigated in ultrahigh vacuum (10^{-9} Torr) at an elevated temperature of ~200 °C in order to increase conductivity of the films. Electronic transport measurements were performed in a physical property measurement system (Quantum Design) in a four-point van der Pauw geometry for monolithic films and two-point probe to measure anisotropy of heterostructures. Optical absorption measurements were carried out on a variable-angle spectroscopic ellipsometer (J.A. Woollam M2000-U) at five angles (65°, 67.5°, 70°, 72.5°, and 75°) in the photon energy range of 1.25–5 eV. Optical constants Ψ and Δ were converted to refractive index n and extinction coefficient k by WVASE software. A bare LSAT substrate was measured and fit to a Cauchy dispersion relationship. Thin-film samples were measured and fit to a model using a homogeneous film with thickness determined by x-ray reflectivity on the LSAT substrate. Optical constants n and k were extracted from the film by fitting the model to the data using Tauc-Lorentz, Drude, and Gaussian oscillators. Optical absorption (α) was calculated using the relationship $\alpha = 4\pi k\lambda^{-1}$, where λ is the photon wavelength.

III. RESULTS AND DISCUSSION

Films of reduced strontium ferrate were grown by oxygen-assisted molecular beam epitaxy on LSAT substrates. In bulk $Sr_2Fe_2O_5$, the brownmillerite structure can be confirmed through the existence of half-order peaks in the full XRD scan, but for films under compressive strain, as is the case for $SrFeO_{2.5}$ on LSAT, the oxygen vacancies order along adjacent (100) planes, thereby doubling the in-plane unit cell [54]. Therefore, $SrFeO_{2.5}$ films grown on (001)-oriented LSAT will not show half-order peaks in 00L XRD scans. While XRD experiments could not confirm the brownmillerite structure, they yielded an out-of-plane lattice parameter of 4.016 Å, consistent with previously reported brownmillerite $SrFeO_{2.5}$ films [55]. The electronic and optical properties of the as-grown films, described later in this paper, are also indicative of a film with oxygen composition of or near $SrFeO_{2.5}$.

In the patterning process, direct-writing photolithography was used to deposit a hard mask of chromium or copper in the desired pattern onto a $SrFeO_{2.5}$ film (Fig. 1). Hard-mask deposition was followed by an ozone anneal to achieve the $SrFeO_{2.5}/SrFeO_3$ ($SFO_{2.5}/SFO_3$) lateral heterostructure, or alternatively a fluorination reaction using PVDF as the fluorine source to achieve the $SrFeO_{2.5}/SrFeO_2F$ ($SFO_{2.5}/SFO_2F$) lateral heterostructure. In the final step, a wet etch was used to remove the Cr or Cu hard mask. Further details of the topochemical process are found in the Supplemental Material [52] (Fig. S1). To obtain a $SrFeO_3/SrFeO_2F$ (SFO_3/SFO_2F) lateral heterostructure, the $SFO_{2.5}/SFO_2F$ sample was then subjected to an ozone anneal, as the fluoride ions were found to be effectively immobile once incorporated into the films with respect to subsequent low-temperature anneals in ambient and O_2/O_3 atmospheres.

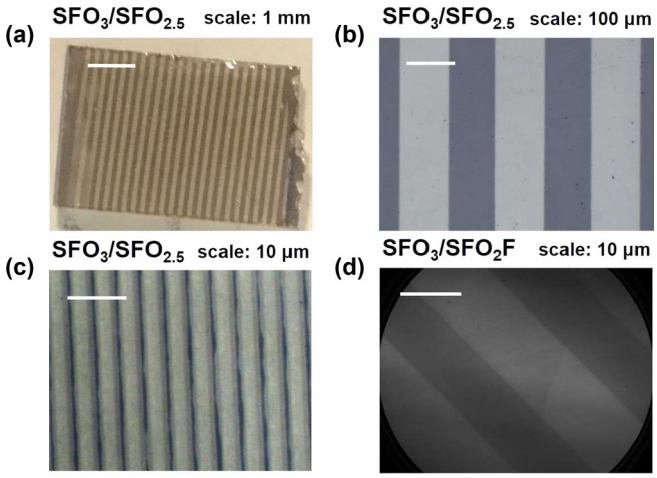

FIG. 2. Optical micrographs of (a) a 200-μm periodicity $SFO_3/SFO_{2.5}$ heterostructure, (b) a 200-μm periodicity $SFO_3/SFO_{2.5}$ heterostructure, and (c) a 4-μm periodicity $SFO_3/SFO_{2.5}$ heterostructure. (d) A PEEM image measured at 690 eV, on the F K-edge, of a 20-μm periodicity SFO_3/SFO_2F heterostructure. Scale bars are included.

Optical microscopy images of the various patterned films are shown in Figs. 2(a)–2(c). Figure 2(a) displays a ~5 × 5 mm^2 film patterned with striped periodic regions 200 μm in width of $SFO_3/SFO_{2.5}$ with distinct regions of SFO_3 and $SFO_{2.5}$. Micrographs of the patterned films at higher magnification also reveal the disparity of phases in 200-μm striped $SFO_3/SFO_{2.5}$ [Fig. 2(b)] and 4-μm striped $SFO_3/SFO_{2.5}$ [Fig. 2(c)]. Figure 2(d) shows a PEEM image of a 20-μm striped $SFO_{2.5}/SFO_2F$ heterostructure measured at the F K-edge, 690 eV. The brighter areas are the regions containing fluorine, SFO_2F, while the darker areas are those without, $SFO_{2.5}$. XAS measurements further corroborate the containment of fluorine within the lateral stripes through comparison of F K-edge and O K-edge spectra in the light and dark regions, revealing a fluorine signal and lower oxygen signal in the light region (Fig. S2, Supplemental Material [52]). We note that while the features are clearly defined in the low-magnification micrographs shown in Fig. 2, the interfaces are not atomically abrupt, as lateral diffusion of O and F occurs along with vertical diffusion of ions during the topochemical reactions.

The coexistence of the two distinct phases and their crystallographic integrity within the patterned films was examined using XRD. Figure 3 shows comparisons of the 002 diffraction peaks measured in the monolithic pure phases and their respective heterostructured combinations, prepared with a Cr hard mask. On the LSAT substrate (a = 3.868 Å), $SrFeO_{2.5}$ has an out-of-plane (c-axis) lattice parameter of 4.016 Å. Upon oxidation, the c-axis parameter shrinks ~3.8% to 3.861 Å. Upon fluorination, SFO_2F has a ~0.8% expanded

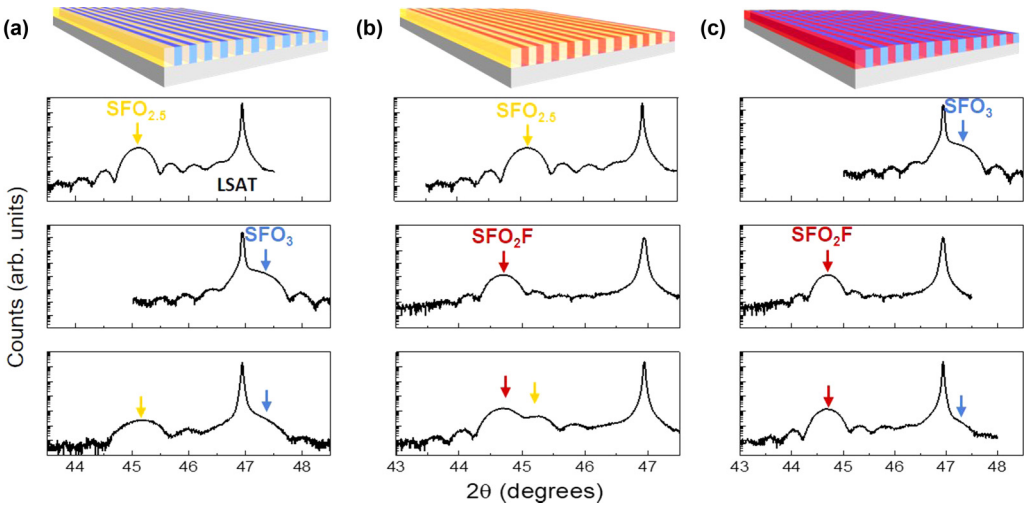

FIG. 3. X-ray diffraction measured from (a) $SFO_{2.5}/SFO_3$, (b) $SFO_{2.5}/SFO_2F$, and (c) SFO_3/SFO_2F heterostructures (bottom panels) with data from monolithic constituent phases shown in the top and middle panels for reference.

lattice parameter of 4.051 Å. To the best of our knowledge, SFO_2F films have not been previously reported on LSAT, but the expansion of the out-of-plane lattice parameter is consistent with previously reported SFO_2F films on $SrTiO_3$ substrates synthesized with a similar vapor transport fluorination approach [47,50].

In the lateral heterostructures, XRD data show a superposition of the constituent phases, confirming the coexistence of the phases. After ozone annealing the $SFO_{2.5}/SFO_2F$ heterostructure [Fig. 3(b)] to achieve the SFO_3/SFO_2F heterostructure [Fig. 3(c)], there is no shift in the position of the SFO_2F diffraction peak, signifying no appreciable fluorine loss. We therefore conclude that the fluorine ions are immobile at the temperature of the ozone anneal (∼150 °C). We note that the film peak of the phase that was covered by the Cr hard mask during lithography [$SFO_{2.5}$ in Figs. 3(a) and 3(b), and SFO_3 in Fig. 3(c)] exhibits some peak broadening (∼27%) in relation to unreacted phase, indicating a decrease in the coherence length of the film [56]. Upon investigation of the surface chemistry of patterned films using PEEM, agglomerates were seen on the surface that we associate with a phase separation of SrO at the surface layer, as supported by XAS spectra shown in Fig. S2 (Supplemental Material [52]). We hypothesize that the phase separation is potentially caused by the high temperature of deposition and anodic tendency of Cr. Further discussion can be found in the Supplemental Material [52]. Accordingly, the use of a Cu hard mask is found to mitigate the formation of these undesired phases and enables lateral heterostructures with no apparent degradation of crystallinity as determined by XRD. The XRD data and simulations of a SFO_3/SFO_2F heterostructure fabricated with a Cu mask are shown in Fig. 4, confirming the absence of XRD peak broadening between the two phases. Atomic force microscopy measurements of a $SFO_{2.5}/SFO_2F$ heterostructure processed using a Cu mask are shown in Fig. S3 in the Supplemental Material [52].

Having established the ability to form oxide-based lateral heterostructures, we turn to the functional properties of these systems. Electronic transport properties of the patterned films were measured to confirm anisotropy within the lateral heterostructures. Figure 5 (top panel) shows the resistivity as a function of temperature for pure $SFO_{3-\delta}$ ($\delta \approx 0.5$), an insulator, and SFO_3, a metal. The bottom panel of Fig. 5 shows the results of two-point probe resistance measurements in a 200-μm period $SFO_3/SFO_{2.5}$ heterostructure. As would be expected, the lateral heterostructure displays low resistance when current flows parallel to the metallic SFO_3 stripes and insulating behavior when measured perpendicular to the stripes, with the alternating $SFO_{2.5}$ and SFO_3 regions essentially acting as resistors in series. The reproducibility of the results are shown in Fig. S4 (Supplemental Material [52]), and the material quality is further corroborated in that the parallel resistance data retain a resistive feature near 110 K that we attribute to the onset of helical magnetic ordering in SFO_3 (Fig. S5, Supplemental Material [52]) [55]. Electronic anisotropy is a result of the chosen geometry of parallel metal-oxide stripes, but other geometries and materials systems could also be selected for ionic and thermal anisotropy, or alternative targeted properties and phenomena based on lateral arrays.

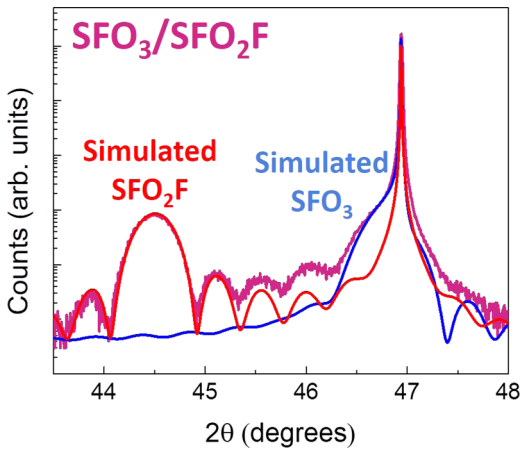

FIG. 4. X-ray diffraction of SFO_3/SFO_2F heterostructure (purple) with superimposed simulated diffraction data of SFO_3 (blue) and SFO_2F (red).

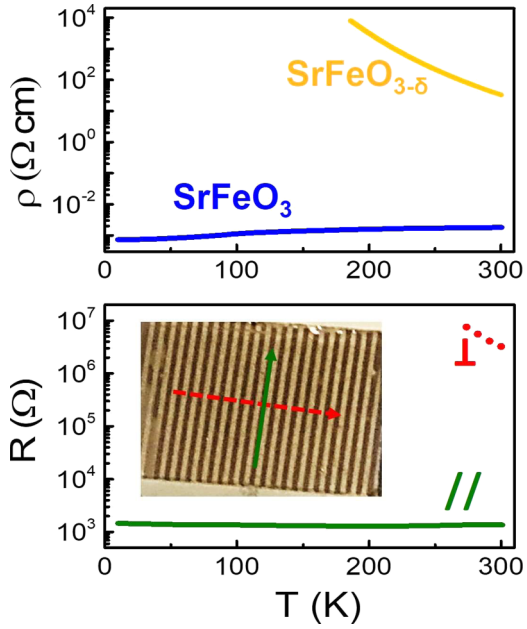

FIG. 5. Electronic resistivity as a function of temperature for monolithic insulating $SFO_{3-\delta}$ ($\delta \approx 0.5$) and metallic SFO_3 (top), and resistance as a function of temperature for a 200-μm periodicity $SFO_3/SFO_{2.5}$ heterostructure (bottom) measured perpendicular to the stripe direction (red, dotted) and parallel to the stripe direction (green, solid), with inset visualization of current direction in a film.

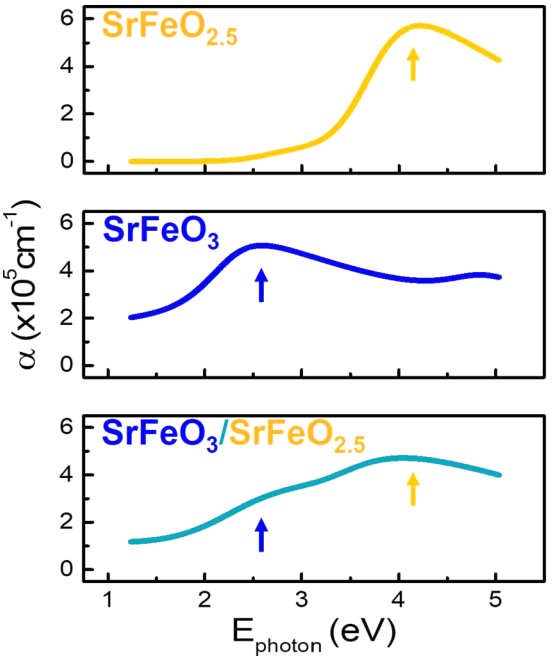

FIG. 6. Optical absorption spectra of monolithic $SFO_{2.5}$ (top), SFO_3 (middle), and of the 200-μm periodicity $SFO_3/SFO_{2.5}$ heterostructure (bottom).

Oxide thin films have demonstrated use as optical waveguides [57,58], and therefore lateral heterostructured films could prove useful for optical applications such as Bragg reflectors [59], resonance filters [60], plasmonic waveguides, and diffraction gratings. Vital to predicting use for these applications is the prerequisite that constituent layers maintain their pure-phase optical properties. Optical absorption data from monolithic $SFO_{2.5}$, SFO_3, and a 200-μm period striped $SFO_3/SFO_{2.5}$ heterostructure are presented in Fig. 6, which confirm that the constituent layers retain their optical response within the heterostructure. As expected of $SFO_{2.5}$, the phase-pure film is transparent in a large portion of the visible spectrum (Fig. 6, top) with a band gap of ∼2.3 eV, in agreement with calculated values for $SrFeO_{2.5}$ epitaxially strained on LSAT [54], and exhibits a major absorptive feature at 4.25 eV. Also in agreement with theoretical and experimental values [49], SFO_2F has an increased band gap of ∼2.4 eV (Fig. S6, Supplemental Material [52]). SFO_3 absorbs across the entire spectrum (Fig. 6, middle), as expected of a metal, with a major absorptive feature at 2.6 eV. The absorption spectrum of the $SFO_3/SFO_{2.5}$ heterostructure, shown in Fig. 6 (bottom), contains both major absorptive features of the distinct $SFO_{2.5}$ and SFO_3 phases. No diffractive effects are expected to occur at these wavelengths for the 200-μm stripe periodicity of this sample; however, we anticipate that diffraction gratings can be engineered from similar heterostructures with smaller periodicities. Spectra measured with ellipsometer beam elongation parallel to the stripes and perpendicular to the stripes were equivalent (Fig. S7, Supplemental Material [52]). This optical characterization further confirms that constituent layers in the laterally heterostructured films retain their pure-phase properties when patterned with this approach.

The topochemical reduction and oxidation processes within the heterostructures enable the erasure and reformation of patterns. This functionality is demonstrated in Fig. 7, which shows XRD data and optical micrographs of a heterostructured film cycled between $SFO_{2.5}/SFO_2F$ and SFO_3/SFO_2F, illustrating the generation, erasure, and regeneration of the metal-insulator pattern. The conversion from SFO_3/SFO_2F to $SFO_{2.5}/SFO_2F$ occurs by heating the sample at ∼250 °C in air, during which oxygen is spontaneously lost from the SFO_3 layers. The SFO_2F phase remains nominally unchanged, while the metallic SFO_3 regions are thermally reduced to the electronically insulating and optically transparent $SFO_{2.5}$ phase. Figure S8 (Supplemental Material [52]) shows the erasure of the metallic stripes in an SFO_3/SFO_2F heterostructure during a thermal anneal at ∼250 °C over time. The oxidation back to SFO_3/SFO_2F is realized through subsequent ozone annealing of the $SFO_{2.5}/SFO_2F$ pattern.

In this demonstration of reconfigurability, the significance of the fluorinated heterostructure lies in the effective permanence of the fluorine pattern in the films under these reaction conditions. As such, the films can be annealed in air and ozone to cyclically erase and recover the metal-insulator pattern, bypassing the need for further lithography. This switching could potentially be realized in the form of a solid-state ionic gating [61–63] or ionic liquid gating [64,65] to cycle the heterostructure using an electrical potential and oxygen conductor instead of ozone. Of note for any practical application, $SrFeO_3$ tends to spontaneously lose oxygen at room temperature over a timescale of days to weeks, but binary oxide capping layers have been shown to prevent spontaneous oxygen loss [66]. Similar capping layers could be utilized on

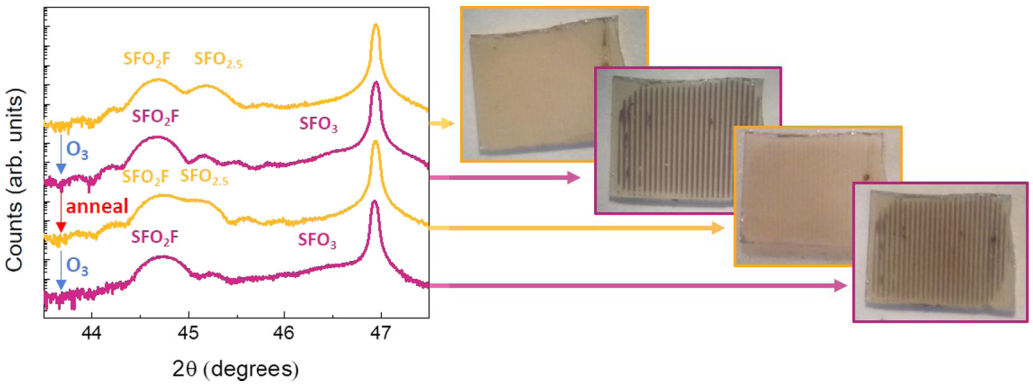

FIG. 7. XRD data and optical microscope images of a 200-μm period $SFO_{2.5}/SFO_2F$ heterostructured film undergoing a sequence of oxidation and thermal reduction (~250 °C) steps, demonstrating reconfigurable pattern behavior.

lateral heterostructures to increase material stability, with the ion-conducting gate layer potentially also playing this role. The operating temperatures of SFO-derived devices would then be limited by minimalizing lateral ionic diffusion, which motivates detailed future studies of oxygen and fluorine in-plane diffusion kinetics in perovskite oxides and oxyfluorides. We also envision that new patterns can be reconfigured in all-oxide heterostructures, such as $ABO_{2.5}/ABO_3$, by reducing the whole structure back to $ABO_{2.5}$ and then carrying out a new lithographic patterning step.

IV. CONCLUSION

A technique for lateral patterning of oxide thin-film materials was presented using hard-mask-facilitated topochemical anionic manipulation of strontium ferrate thin films. Striped heterostructures with distinct material phases consisting of oxidized, reduced, and fluorinated SFO were produced with periodicities of 4–200 μm. Microscopy, diffraction, and optical spectroscopy confirm the coexistence of distinct phases, and anisotropic electronic transport properties were elicited. In $SrFeO_3/SrFeO_2F$ and $SrFeO_{2.5}/SrFeO_2F$ heterostructures, pattern erasure and regeneration was demonstrated through low-temperature oxidation and reduction reactions, suggesting that these lateral anionic heterostructures are a potential platform for reconfigurable devices. While here we focused on $SrFeO_{3-\delta}$-based heterostructures, the technique should be broadly applicable to any oxide material amenable to a wide range of topochemical transformations [67–69] in which anion substitution or oxygen deficiency can drive property tunability.

ACKNOWLEDGMENTS

B.M.L. and S.J.M. acknowledge the donors of the American Chemical Society Petroleum Research Fund (Grant No. 57071-ND10) for support of this research. J.W. was supported by the National Science Foundation (Grant No. CMMI-1562223). We would like to thank Prof. Caroline Schauer for access to the spectroscopic ellipsometer. This work was carried out in part at the Singh Center for Nanotechnology, which is supported by the NSF National Nanotechnology Coordinated Infrastructure Program under Grant No. NNCI-1542153.

[1] J. Mannhart and D. G. Schlom, Science **327**, 1607 (2010).
[2] D. G. Schlom, J. H. Haeni, J. Lettieri, C. D. Theis, W. Tian, J. C. Jiang, and X. Q. Pan, Mater. Sci. Eng. B **87**, 282 (2001).
[3] H. N. Lee, H. M. Christen, M. F. Chisholm, C. M. Rouleau, and D. H. Lowndes, Nature (London) **433**, 395 (2005).
[4] M. Brahlek, A. S. Gupta, J. Lapano, J. Roth, H.-T. Zhang, L. Zhang, R. Haislmaier, and R. Engel-Herbert, Adv. Funct. Mater. **28**, 1702772 (2018).
[5] N. Yu and F. Capasso, Nat. Mater. **13**, 139 (2014).
[6] C. M. Soukoulis and M. Wegener, Nat. Photonics **5**, 523 (2011).
[7] J. Salman, M. Hafermann, J. Rensberg, C. Wan, R. Wambold, B. S. Gundlach, C. Ronning, and M. A. Kats, Adv. Opt. Mater. **6**, 1701027 (2018).
[8] R. Anufriev, A. Ramiere, J. Maire, and M. Nomura, Nat. Commun. **8**, 15505 (2017).
[9] X. Duan, C. Wang, J. C. Shaw, R. Cheng, Y. Chen, H. Li, X. Wu, Y. Tang, Q. Zhang, A. Pan, J. Jiang, R. Yu, Y. Huang, and X. Duan, Nat. Nanotechnol. **9**, 1024 (2014).
[10] G. Fiori, A. Betti, S. Bruzzone, and G. Iannaccone, ACS Nano **6**, 2642 (2012).
[11] E. Y. Cho, Y. W. Zhou, J. Y. Cho, and S. A. Cybart, Appl. Phys. Lett. **113**, 022604 (2018).
[12] M. Nijland, A. George, S. Thomas, E. P. Houwman, J. Xia, D. H. A. Blank, G. Rijnders, G. Koster, and J. E. ten Elshof, Adv. Funct. Mater. **24**, 6853 (2014).
[13] C. A. Ross, Annu. Rev. Mater. Res. **31**, 203 (2001).
[14] R. Ruiz, E. Dobisz, and T. R. Albrecht, ACS Nano **5**, 79 (2011).
[15] Y. Zhou, S. Li, Y. Wang, Q. Huang, W. Zhang, Y. Yao, J. Hao, Y. Sun, M. Tang, B. Li, Y. Zhang, J. Hu, and L. Yan, Carbon **148**, 387 (2019).
[16] S. Lee and J. L. MacManus-Driscoll, APL Mater. **5**, 042304 (2017).
[17] C. Cen, S. Thiel, J. Mannhart, and J. Levy, Science **323**, 1026 (2009).
[18] P. Irvin, J. P. Veazey, G. Cheng, S. Lu, C.-W. Bark, S. Ryu, C.-B. Eom, and J. Levy, Nano Lett. **13**, 364 (2013).

[19] Y. Wang, K. Zhao, X. Shi, G. Li, G. Xie, X. Lai, J. Ni, and L. Zhang, Sci. Rep. **5**, 10841 (2015).

[20] P. P. Aurino, A. Kalabukhov, N. Tuzla, E. Olsson, T. Claeson, and D. Winkler, Appl. Phys. Lett. **102**, 201610 (2013).

[21] S. Mathew, A. Annadi, T. K. Chan, T. C. Asmara, D. Zhan, X. R. Wang, S. Azimi, Z. Shen, A. Rusydi, Ariando, M. B. H. Breeze, and T. Venkatesan, ACS Nano **7**, 10572 (2013).

[22] R. V. Chopdekar, B. Li, T. A. Wynn, M. S. Lee, Y. Jia, Z. Q. Liu, M. D. Biegalski, S. T. Retterer, A. T. Young, A. Scholl, and Y. Takamura, Phys. Rev. Mater. **1**, 024401 (2017).

[23] Y. Takamura, R. V. Chopdekar, A. Scholl, A. Doran, J. A. Liddle, B. Harteneck, and Y. Suzuki, Nano Lett. **6**, 1287 (2006).

[24] A. Herklotz, S. F. Rus, N. Balke, C. Rouleau, E.-J. Guo, A. Huon, Santosh KC, R. Roth, X. Yang, C. Vaswani, J. Wang, P. P. Orth, M. S. Scheurer, and T. Z. Ward, Nano Lett. **19**, 1033 (2019).

[25] A. Herklotz, Z. Gai, Y. Sharma, A. Huon, S. F. Rus, L. Sun, J. Shen, P. D. Rack, and T. Z. Ward, Adv. Sci. **5**, 1800356 (2018).

[26] S. Saremi, R. Xu, L. R. Dedon, J. A. Mundy, S.-L. Hsu, Z. Chen, A. R. Damodaran, S. P. Chapman, J. T. Evans, and L. W. Martin, Adv. Mater. **28**, 10750 (2016).

[27] H. Zheng, J. Wang, S. E. Lofland, Z. Ma, L. Mohaddes-Ardabili, T. Zhao, L. Salamanca-Riba, S. R. Shinde, S. B. Ogale, F. Bai, D. Viehland, Y. Jia, D. G. Schlom, M. Wuttig, A. Roytburd, and R. Ramesh, Science **303**, 661 (2004).

[28] F. Zavaliche, T. Zhao, H. Zheng, F. Straub, M. P. Cruz, P. L. Yang, D. Hao, and R. Ramesh, Nano Lett. **7**, 1586 (2007).

[29] W. Zhang, J. Jian, A. Chen, L. Jiao, F. Khatkhatay, L. Li, F. Chu, Q. Jia, J. L. MacManus-Driscoll, and H. Wang, Appl. Phys. Lett. **104**, 062402 (2014).

[30] A. Chen, W. Zhang, F. Khatkatay, Q. Su, C. F. Tsai, L. Chen, Q. X. Jia, J. L. Macmanus-Driscoll, and H. Wang, Appl. Phys. Lett. **102**, 093114 (2013).

[31] W. Ma, J. J. Kim, N. Tsvetkov, T. Daio, Y. Kuru, Z. Cai, Y. Chen, K. Sasaki, H. L. Tuller, and B. Yildiz, J. Mater. Chem. A **3**, 207 (2015).

[32] J. L. MacManus-Driscoll, P. Zerrer, H. Wang, H. Yang, J. Yoon, A. Fouchet, R. Yu, M. G. Blamire, and Q. Jia, Nat. Mater. **7**, 314 (2008).

[33] A. Chen, Q. Su, H. Han, E. Enriquez, and Q. Jia, Adv. Mater. **31**, 1803241 (2019).

[34] P. Adler, A. Lebon, V. Damljanović, C. Ulrich, C. Bernhard, A. V. Boris, A. Maljuk, C. T. Lin, and B. Keimer, Phys. Rev. B **73**, 094451 (2006).

[35] T. Das, J. D. Nicholas, and Y. Qi, J. Mater. Chem. A **5**, 4493 (2017).

[36] E. Enriquez, A. Chen, Z. Harrell, P. Dowden, N. Koskelo, J. Roback, M. Janoschek, C. Chen, and Q. Jia, Sci. Rep. **7**, 46184 (2017).

[37] C. Greaves, A. J. Jacobson, B. C. Tofield, and B. E. F. Fender, Acta Crystallogr., Sect. B: Struct. Crystallogr. Cryst. Chem. **31**, 641 (1975).

[38] A. Khare, D. Shin, T. S. Yoo, M. Kim, T. D. Kang, J. Lee, S. Roh, I. Jung, J. Hwang, S. W. Kim, T. W. Noh, H. Ohta, and W. S. Choi, Adv. Mater. **29**, 1606566 (2017).

[39] A. Lebon, P. Adler, C. Bernhard, A. V. Boris, A. V. Pimenov, A. Maljuk, C. T. Lin, C. Ulrich, and B. Keimer, Phys. Rev. Lett. **92**, 037202 (2004).

[40] Z. Li, R. Laskowski, T. Iitaka, and T. Tohyama, Phys. Rev. B **85**, 134419 (2012).

[41] V. V. Vashuk, L. V. Kokhanovskii, and I. I. Yushkevich, Inorg. Mater. **36**, 79 (2000).

[42] Y. Xie, M. D. Scafetta, R. J. Sichel-Tissot, E. J. Moon, R. C. Devlin, H. Wu, A. L. Krick, and S. J. May, Adv. Mater. **26**, 1434 (2014).

[43] H. D'Hondt, A. M. Abakumov, J. Hadermann, A. S. Kalyuzhnaya, M. G. Rozova, E. V. Antipov, and G. Van Tendeloo, Chem. Mater. **20**, 7188 (2008).

[44] W. Paulus, H. Schober, S. Eibl, M. Johnson, T. Berthier, O. Hernandez, M. Ceretti, M. Plazanet, K. Conder, and C. Lamberti, J. Am. Chem. Soc. **130**, 16080 (2008).

[45] M. V. Patrakeev, I. A. Leonidov, V. L. Kozhevnikov, and V. V. Kharton, Solid State Sci. **6**, 907 (2004).

[46] E. J. Moon, Y. Xie, E. D. Laird, D. J. Keavney, C. Y. Li, and S. J. May, J. Am. Chem. Soc. **136**, 2224 (2014).

[47] T. Katayama, A. Chikamatsu, Y. Hirose, R. Takagi, H. Kamisaka, T. Fukumura, and T. Hasegawa, J. Mater. Chem. C **2**, 5350 (2014).

[48] F. J. Berry, X. Ren, R. Heap, P. Slater, and M. F. Thomas, Solid State Commun. **134**, 621 (2005).

[49] T. Katayama, A. Chikamatsu, H. Kamisaka, H. Kumigashira, and T. Hasegawa, Appl. Phys. Express **9**, 025801 (2016).

[50] E. J. Moon, A. K. Choquette, A. Huon, S. Z. Kulesa, D. Barbash, and S. J. May, APL Mater. **3**, 062511 (2015).

[51] C. M. Thompson, C. K. Blakely, R. Flacau, J. E. Greedan, and V. V. Poltavets, J. Solid State Chem. **219**, 173 (2014).

[52] See Supplemental Material at http://link.aps.org/supplemental/10.1103/PhysRevMaterials.3.073802 for a schematic of the postgrowth topochemical reaction setup, PEEM, XAS, and AFM measurements from heterostructures, additional anisotropic electronic transport measurements of $SFO_3/SFO_{2.5}$ heterostructures, a temperature-dependent resistance data comparison of pure-phase SFO_3 and an $SFO_3/SFO_{2.5}$ heterostructure with transport measured parallel to the striped pattern, optical absorption spectra of $SFO_{2.5}$ and SFO_2F, heterostructure absorption spectra measured at varied incidence with respect to the heterostructure geometry, and time-lapse images of a heterostructure pattern erasure. Supplemental Material includes Refs. [34,47,70,71].

[53] M. Björck and G. Andersson, J. Appl. Crystallogr. **40**, 1174 (2007).

[54] J. Young and J. M. Rondinelli, Phys. Rev. B **92**, 174111 (2015).

[55] H. Yamada, M. Kawasaki, and Y. Tokura, Appl. Phys. Lett. **80**, 622 (2002).

[56] A. L. Patterson, Phys. Rev. **56**, 978 (1939).

[57] F. J. Walker, R. A. McKee, H. W. Yen, and D. E. Zelmon, Appl. Phys. Lett. **65**, 1495 (1994).

[58] P. K. Tien, Appl. Opt. **10**, 2395 (1971).

[59] J. W. Leem, X.-Y. Guan, and J. S. Yu, Opt. Express **22**, 18519 (2014).

[60] H.-A. Lin and C.-S. Huang, IEEE Photonics Technol. Lett. **28**, 1042 (2016).

[61] D. Chen and H. L. Tuller, Adv. Funct. Mater. **24**, 7638 (2014).

[62] U. Bauer, L. Yao, A. J. Tan, P. Agrawal, S. Emori, H. L. Tuller, S. van Dijken, and G. S. D. Beach, Nat. Mater. **14**, 174 (2015).

[63] A. L. Krick and S. J. May, APL Mater. **5**, 042504 (2017).

[64] B. Cui, P. Werner, T. Ma, X. Zhong, Z. Wang, J. M. Taylor, Y. Zhuang, and S. S. P. Parkin, Nat. Commun. **9**, 3055 (2018).

[65] C. Leighton, Nat. Mater. **18**, 13 (2019).

[66] E. Enriquez, A. Chen, Z. Harrell, X. Lü, P. Dowden, N. Koskelo, M. Janoschek, C. Chen, and Q. Jia, Appl. Phys. Lett. **109**, 141906 (2016).

[67] Y. Shimakawa, Bull. Chem. Soc. Jpn. **86**, 299 (2013).

[68] R. Uppuluri, A. Sen Gupta, A. S. Rosas, and T. E. Mallouk, Chem. Soc. Rev. **47**, 2401 (2018).

[69] J. Gopalakrishnan, Chem. Mater. **7**, 1265 (1995).

[70] J. A. McLeod, R. G. Wilks, N. A. Skorikov, L. D. Finkelstein, M. Abu-Samak, E. Z. Kurmaev, and A. Moewes, Phys. Rev. B **81**, 245123 (2010).

[71] S.-I. Nakai, T. Mitsuishi, H. Sugawara, H. Maezawa, T. Matsukawa, S. Mitani, K. Yamasaki, and T. Fujikawa, Phys. Rev. B **36**, 9241 (1987).